DOI 10.4430/bgo00388

Determination of the relationship between Rare Earth Element (REE) mineralisation and major faults using fractal modelling in the Gazestan deposit, central Iran

M. Nabilou[1], P. Afzal[2], M. Arian[1], A. Adib[2], A. Kazemi Mehrnia[3], M. Jami[4], H. Kheyrollahi[5], M.R. Akhavan Aghdam[5], A. Ameri[5] and L. Daneshvar Saein[6]

[1] *Department of Geology, Islamic Azad University, Tehran, Iran*
[2] *Department of Petroleum and Mining Engineering, Islamic Azad University, Tehran, Iran*
[3] *Department of Geology, Islamic Azad University, Mahalat, Iran*
[4] *Petroleum and Chemical Engineering, Universiti Teknologi Brunei, Bandar Seri Begawan, Brunei Darussalam*
[5] *Division of Airborne Geophysics, Department of Geomatics, Geological Survey of Iran, Tehran, Iran*
[6] *Department of Geology, Payame Noor University, Tehran, Iran*

(Received: 22 October 2021; accepted: 18 March 2022; published online: 27 July 2022)

ABSTRACT The aim of this study is to determine the relationship between Rare Earth Element (REE) mineralisation and major faults in the Gazestan deposit, Bafq metallogenic zone, central Iran, using the Concentration-Distance to Main Fault (C-DMF) fractal model. The C-DMF fractal model is employed for the separation of REE mineralisation based on their distance to major faults obtained by geophysical and drill core data. Major faults were extracted from a geological map, drill cores, and airborne/ground survey magnetometric geophysical data. The C-DMF model of the Gazestan deposit reveals that the main REE mineralisation shows a good correlation to the distance to major faults. Accordingly, the distances of the high REE mineralisation (1251 ppm < REEs ≤ 3091 ppm) show the distance of 6-220 m to the nearest fault. Consequently, the REE concentrations of 1474-2879, 1187-2870, 1419-1628, and 1295-1597 ppm occur at distances of 50-409, 66.8-146, 5-121, and 7-38 m to major magnetic faults in the depth of 50, 100, 150, and 300 m depth horizons. High concentrations of REEs are 2870-3091 ppm, which have distances between 6-90 m to the major magnetic fault in total depths of 50, 100, 150, and 300 m. The Gazestan fault, the major magnetic fault in the area, shows the highest correlation with high REE concentrations. Finally, the C-DMF fractal model can be adopted as a suitable method for separating main mineralisation and detecting the relationship between faults and mineralised zones.

Key words: Concentration-Distance to Main Fault (C-DMF) fractal model, Rare Earth Element (REE) mineralisation, major fault, Gazestan, Iran.

1. Introduction

During the last decades, geologists, geochemists and mining engineers have been using fractal and multifractal models to understand and quantify the spatial distribution of geochemical data to recognise their patterns (Cohen *et al.*, 2010).

Geochemical anomalies generally occur through various ore-forming processes, which are affected by common geological processes. The patterns of geochemical anomalies depend on two major factors: the frequency and spatial distribution of geochemical data, and the geometrical characteristics and scale invariance of geochemical patterns (Agterberg, 1995; Agterberg *et al*., 1996; Davis, 2002; Lima *et al.*, 2003; Carranza, 2009; Afzal *et al.*, 2011, 2012; Zuo *et al.*, 2013; Fyzollahhi *et al.*, 2018; Karaman *et al.*, 2021). In many cases, geochemical anomalies occur with a particular geometry, controlled by particular geological structures such as faults, folds, and joints (Shahabpour, 2010; Mohebi *et al.*, 2015; Adib *et al.*, 2017a, 2017b; Daneshvar Saein and Afzal, 2017; Ahmadfaraj *et al.*, 2019).

Historically, the most common method for geochemical anomalies detection are the definition of a threshold value (Hawkes and Webb, 1979), geochemical data analysis (Carranza, 2010), multivariate statistics, which is based on the frequency distribution of geochemical data without considering spatial variation (Yousefi *et al.*, 2012, 2014; Zuo *et al.*, 2013), and the frequency-space-based methods such as the inverse distance-weighted and kriging methods (Lam, 1983; Journel, 1993; Tahmasebi and Hezarkhani, 2012). The main strength of the fractal/multifractal method is its capacity to quantify irregular distributions that show similarity over a wide range of scales, also known as self-similarity (Mandelbrot, 1983; Zuo and Wang, 2016).

In addition to the scaling characteristics of geochemical data, several fractal and multifractal models were developed. Cheng *et al.* (1994) proposed the Concentration-Area (C-A) fractal model as the first major geochemical fractal/multifractal modelling process and in 1999, they developed the Spectrum-Area (S-A) fractal model as a version of the C-A model in the frequency domain, which could recognise overlapping data using more than one threshold value. Li *et al.* (2003) proposed the Concentration-Distance (C-D) fractal model, which could separate anomalies from the background. Finally, Afzal *et al.* (2011) developed the Concentration-Volume (C-V) fractal model for recognising mineralisation zones.

Cheng (2007) considered mineralisation a singular process and suggested a singularity mapping method to illustrate the exclusivity level of geological features based on the concept that geochemical enrichments are a function of an efficient process (singularity concept). This process was able to distinguish anomalies, which were previously unrecognisable by simple contouring methods (Zuo *et al.*, 2013).

Generally, a geochemical spatial distribution pattern is composed of several sub-patterns with different hierarchical levels. This will produce a spatial geochemical distribution clustered at different scales (Li *et al.*, 2003). Mandelbrot (1983) proposed the radial-density model to characterise the clustering of the points. Using the model and replacing the density with element concentration, Li *et al.* (2003) established the C-D fractal model. The C-D model can estimate the original elemental concentration and prevent any interpolation procedure error. This model can determine the optimum threshold that is fairly similar to the C-A model (Zuo *et al.*, 2013).

The relationship between precious and Rare Earth Element (REE) mineralisation, and geological structures, particularly faults, has been the subject of various studies during the last decades. These studies highlight the significance of structural settings and their influence on mineral deposits (e.g. Craw and Campbell, 2004; Drew, 2006; Wang *et al.*, 2012; Adib *et al.*, 2017a, 2017b; Nabilou *et al.*, 2017; Glorie *et al.*, 2019; Alaminia *et al.*, 2020; Nabilou *et al.*, 2021). Besides geological structures, surface geology and airborne and ground geophysical survey data are important factors in the detection and analysis of faults. The relationship between faults and mineralisation can be quantified using mathematical methods, such as fractal geometry processes. The influence of the ore-forming processes on the ore distribution can be revealed by fractal and multifractal properties and models (Mandelbrot, 1983; Turcotte, 1986; Meng and

Zhao, 1991; Cheng *et al.*, 1994; Agterberg *et al.*, 1996; Li *et al.*, 2003; Ghavami Riabi, 2006; Afzal *et al.*, 2012, 2017, 2018; Khalajmasoumi *et al.*, 2016; Nabilou *et al.*, 2017; Nazarpour, 2018; Farahmandfar *et al.*, 2019; Yasrebi and Hezarkhani, 2019; Alipour Shahsavari *et al.*, 2020). On the other hand, geochemical anomalies, their geometrical properties, and their relationships with geological structures also play an important role in exploration. Fractal methods such as C-A (Cheng *et al.*, 1994), Spectrum-Area (S-A; Cheng, 1999), C-D (Li *et al.*, 2003), C-V (Afzal *et al.*, 2011), Concentration-Distance to Major Fault (C-DMF; Nouri *et al.*, 2013) and Concentration-Number (C-N; Hassanpour and Afzal, 2013) have proved to be effective tools to delineate ore distribution in various geological conditions. Several advanced fractal models were developed by combining with multivariate analysis (Saadati *et al.*, 2020), wavelet transformation (Pourgholam *et al.*, 2021) or mineralographical data (Kouhestani *et al.*, 2020), zonality index (Aliyari *et al.*, 2020) and geostatistical simulation, particularly for REEs and precious metals exploration (Shamseddin Meigooni *et al.*, 2021a, 2021b). Geostatistical simulations have been widely utilised because they predict spatial distribution and analyse spatial and local uncertainty. Also, fractal modelling can be carried out in different simulations (Chen *et al.*, 2013; Madani Esfahani and Asghari, 2013; Soltani *et al.*, 2014; Hajsadeghi *et al.*, 2017; Madani and Carranza, 2020). For example, Sequential Gaussian Simulation (SGS) is widely used to characterise geochemical distribution patterns in this study (Shamseddin Meigooni *et al.*, 2021a, 2021b). One of the advantages of this method is measuring the spatial uncertainty of the unsampled points (Wang and Zuo, 2018, 2019; Liu *et al.*, 2019).

In this study, the C-DMF fractal modelling was employed to recognise the relationship between Fe-P-REE mineralisation and the local faults indicated on the 1:500 Gazestan deposit map and drawn from the airborne and ground magnetometric geophysical data in the Gazestan Fe-oxide-P-REE deposit, Bafq area, Iran.

Moreover, borehole data were used for underground modelling of the main faults and main mineralisation of REEs. The main faults were modelled based on geophysical, geological and drill core data. Then, the main REE mineralisation was separated based on this fractal modelling. Finally, the relationship between REE mineralised zones and the main faults is determined by the C-DMF fractal model.

2. Geological setting

2.1. Regional geology

The central Iran Bafq metalogenic zone hosts several large Fe-oxide, Pb-Zn, U, and P-REE deposits in the lower Cambrian volcanic-sedimentary sequence (Haghipour, 1977; Samani, 1988; Daliran, 2002; Jami, 2005; Sadeghi *et al.*, 2012; Afzali *et al.*, 2014; Heidarian *et al.*, 2017; Deymar *et al.*, 2018; Mehdipour Ghazi *et al.*, 2019; Soltani *et al.*, 2019). With more than 2 billion tons reserve, the majority of Fe-P deposits are classified as Kiruna type with a close spatial and temporal relationship with felsic volcanic rocks (Forster and Jafarzadeh, 1994; Daliran *et al.*, 2007, 2009). These deposits have a special relationship with local and regional faults, described as tectono-magmatic controls (Samani, 1988).

The Gazestan-Fe-oxide-P-REE deposit is located ~78 km east of Bafq city (Fig. 1). The ore deposit is hosted by intrusive and extrusive alkali rhyolites of the epicontinental to continental Infracambrian Esfordi Formation (Afzali *et al.*, 2014, 2017). The studied area is part of the 1:100,000 Esfordi geological map sheet (Soheili and Mahdavi, 1991; Nabilou *et al.*, 2017).

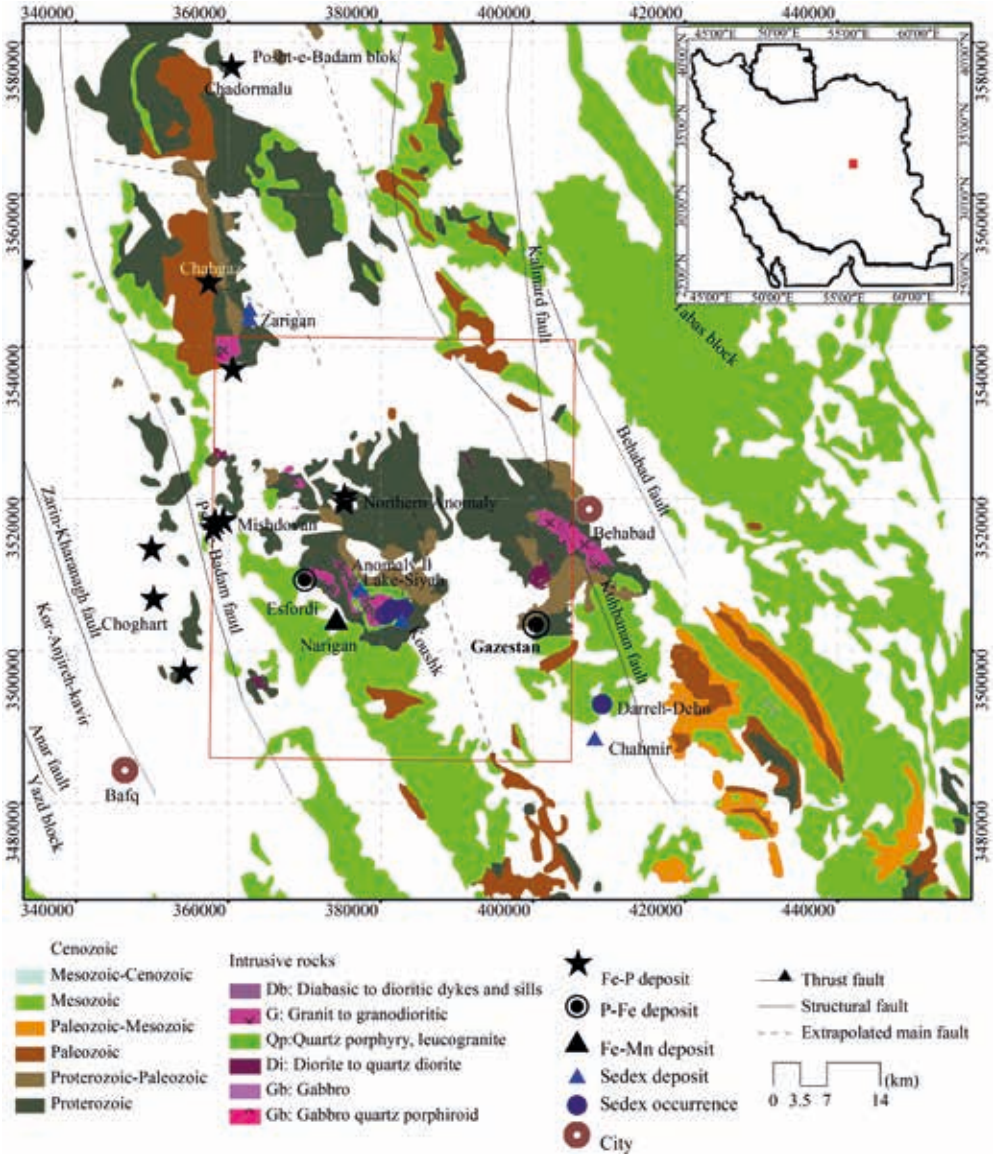

Fig. 1 - Geological map of Posht-e-Badam block and part of the Yazd and Tabas blocks with the major faults (after Rajabi *et al.*, 2012) and ore deposits. The red dashed line rectangle is the extent of the Esfordi 1:100,000 geology map area.

The Precambrian crystalline basement and Early Cambrian to Tertiary sedimentary sequence cover are exposed in the area (Forster and Jafarzadeh, 1994). The Cambrian Volcano Sedimentary Unit (CVSU), as the major host of the Bafq Fe-P-REE deposits, is composed of Rizu-Desu series and Esfordi Formation (Huckriede *et al.*, 1962; Haghipour, 1977; Samani, 1993; Ramezani and Tucker, 2003). The CVSU is made up of felsic tuff, sandstone and micro-conglomerate, mafic, and felsic volcanic rocks, pyritic siltstone-shale, volcanoclastic beds and tuffaceous shale, dolomite and dolomitic limestone (Haghipour, 1974; Ramezani and Tucker, 2003; Jami *et al.*, 2007; Rajabi, 2012; Rajabi *et al.*, 2015; Mehdipour Ghazi *et al.*, 2019).

The Early Cambrian volcano-sedimentary sequence host of the Bafq Fe-P-REE deposits (Fig. 1) are mainly associated with replacement features, brecciation textures, and sodic-calcic alteration

interpreted as iron oxide copper gold ore deposits and Kiruna-type deposits (Forster and Jafarzadeh, 1994; Jami *et al.*, 2007; Daliran *et al.*, 2010; Stosch *et al.*, 2011; Sadeghi *et al.*, 2013).

The Gazestan exploration reports and the 1:5000 geological map show two major host units, a Lower Cambrian sedimentary volcanic series, composed of carbonates, shale-sandstone and rhyolite, trachyte and trachy-andesite and tuff (Fig. 2), and the intrusive rocks including micro-granite and granodiorite (Dori and Jamali, 2003; Dori *et al.*, 2008; Parsi Kankav Consultant Engineers Co., 2015).

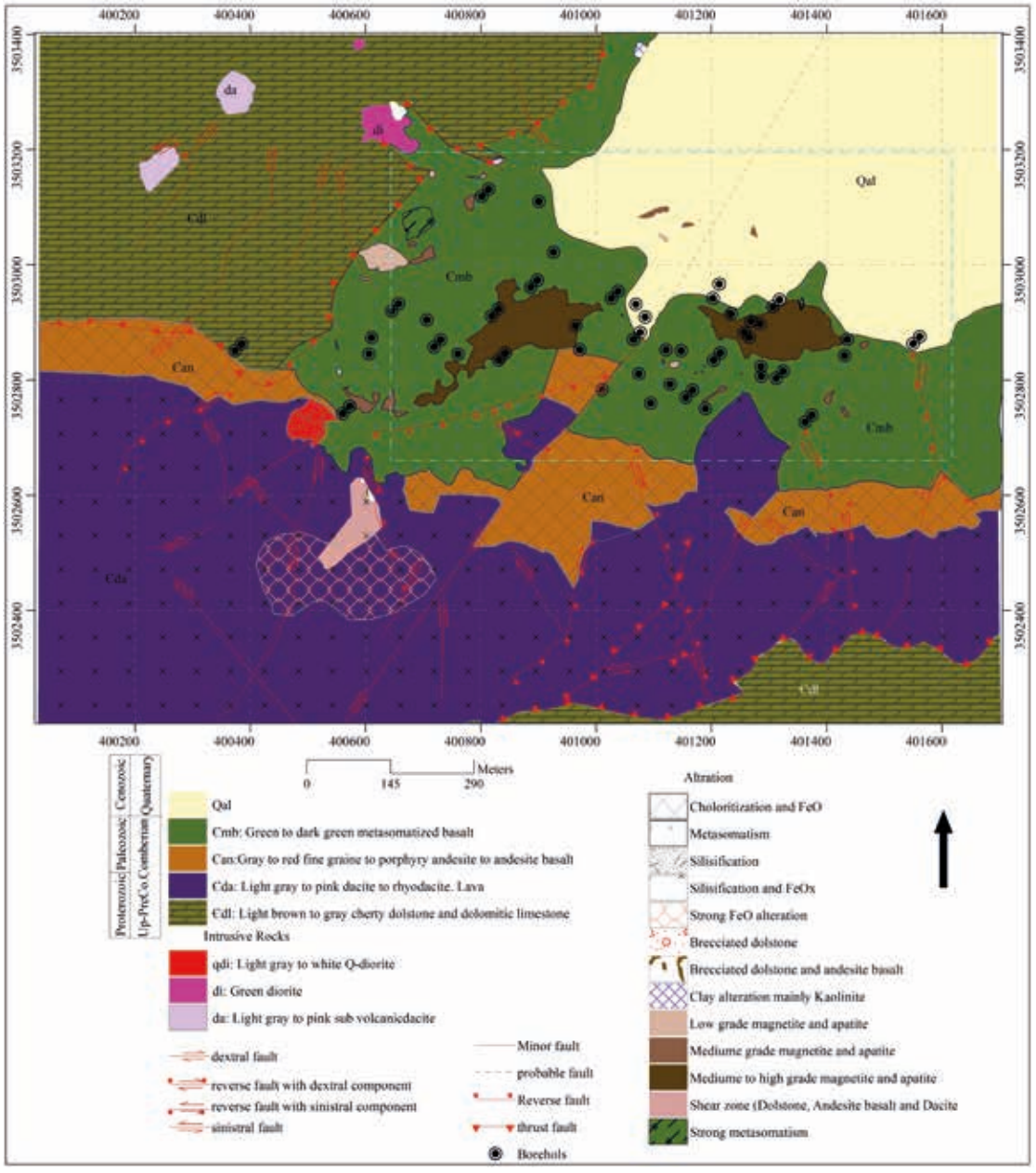

Fig. 2 - 1:5000 geological map of the Gazestan deposit (Parsi Kankav Consultant Engineers Co., 2015). The blue rectangle is the studied deposit.

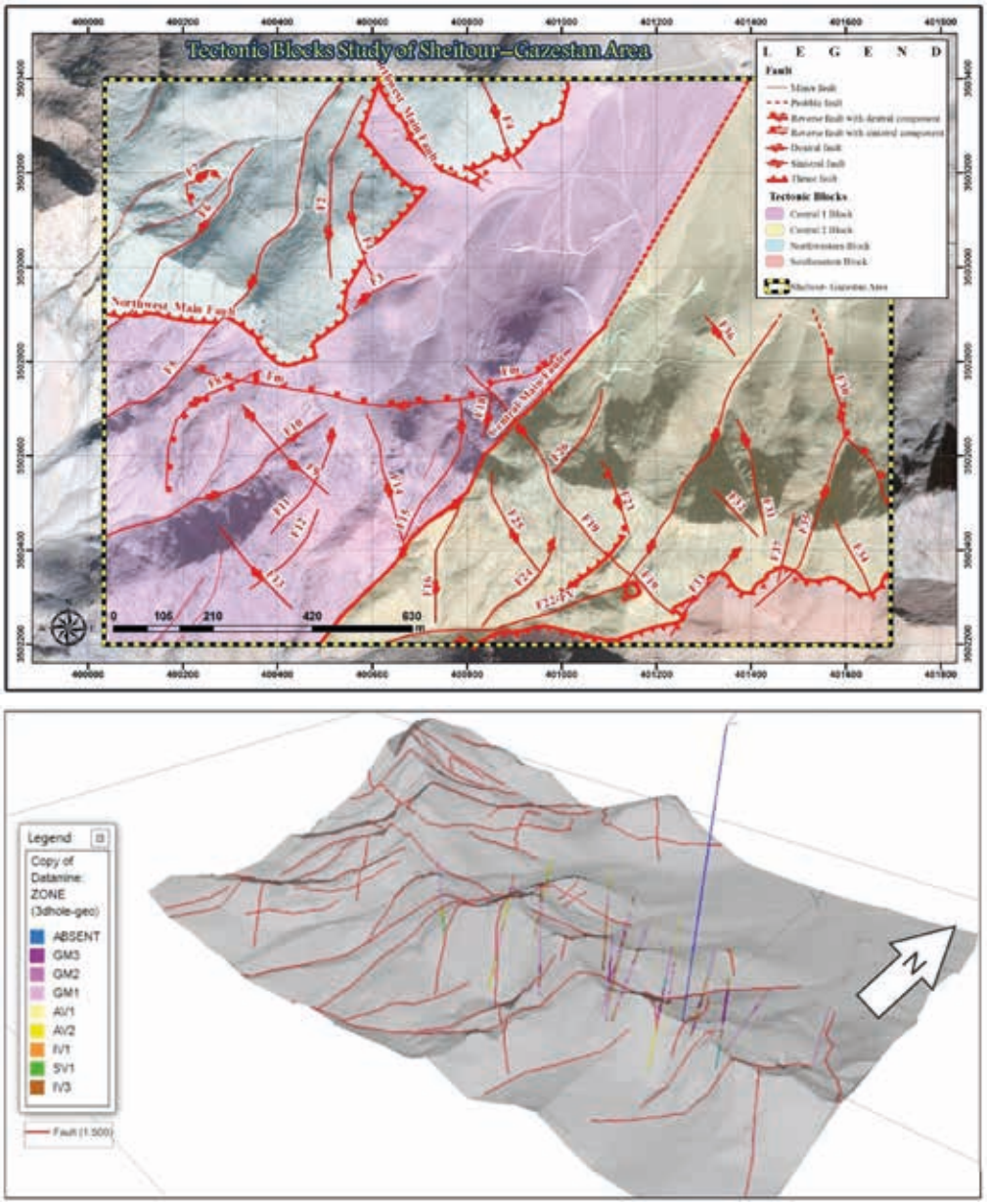

Fig. 3 - 2D and 3D faults map in the Sheitour-Gazestan area (Parsi Kankav Consultant Engineers Co., 2015).

2.2. Structural geology

The structural setting of the Gazestan deposit is linked to the Alpine orogenic phase. Among 40 faults mapped in the Gazestan deposit, three were recognised as main faults (Table 1 and Fig. 3). Fig. 4a shows the Riedel shear patterns (McClay and Bonora, 2001), which indicates that 60% of total faults are correlated with this pattern. Fig. 4b displays the Gazestan faults rose diagram suggesting different fault classes. Riedel shear structures are common fault patterns in shear zones and are related to the primary stages of fault formation. The basic geometry of the Riedel structure consists of conjugate shear bands arranged in *en echelon* arrays. The Gazestan

Table 1 - Detected faults of the Gazestan deposit based on 1:500 geological map.

Displacement of rocks	Slickenline	Strike/Dip	Mechanism	Name Fault
	-	N-S	Dextral Strike Slip	F1
-	-	N-S	Dextral Strike Slip	F2
	-	070/65N	Reverse with Sinistral Strike Slip component	North West Major Fault
	-	NE-SW	Sinistral Strike Slip	F3
	-	NNW-SSE	Reverse with Dextral Strike Slip component	F4
	-	NE-SW	Sinistral Strike Slip with reverse component	F5
	-	NE-SW	Sinistral Strike Slip with reverse component	F6
	-	NE-SW	Reverse with Sinistral Strike Slip component	F7
		035/42NW	Reverse with Dextral Strike Slip component	F8
	-	305/90	Sinistral Strike Slip	F9
-	-	NE-SW	Dextral Strike Slip	F10
		020/67W	Sinistral Strike Slip with reverse component	F11
	-	NE-SW	Sinistral Strike Slip with reverse component	F12
-	-	NW-SE	Dextral Strike Slip	F13
-		155/87E	Dextral Strike Slip with reverse component	F14
	-	N-S	Dextral Strike Slip	F15
	-	N-S	Dextral Strike Slip	F16
	-	N-S	Dextral Strike Slip with Normal component	F17
-	-	NE-SW	Sinistral Strike Slip	F18
	-	NW-SE	Dextral Strike Slip with reverse component	F19
		070/72NW	Reverse with Dextral Strike Slip component	Fm
-	-	NW-SE	Sinistral Strike Slip	F20
	-	NW-SE	Sinistral Strike Slip	F21
	-	NE-SW	Sinistral Strike Slip with reverse component	Fv
	-	NE-SW	Sinistral Strike Slip with reverse component	F22
	-	NNW-SSE	Reverse with Dextral Strike Slip component	F23
	-	NNE-SSW	Dextral Strike Slip with reverse	F24
	-	NNW-SSE	Dextral Strike Slip with reverse component	F25
	-	NE-SW	Dextral Strike Slip	F26
	-	NW-SE	Dextral Strike Slip with reverse component	F27
	-	NNW-SSE	Dextral Strike Slip	F28
	-	N-S	Sinistral Strike Slip	F29
-		150/70SW	Reverse with Dextral Strike Slip component	F30
	-	NW-SE	Dextral Strike Slip with reverse component	F31
-	-	NE-SW	Sinistral Strike Slip with reverse component	F32
		NE-SW	Dextral Strike Slip	F33
	-	NNW-SSE	Sinistral Strike Slip	F34
	-	NE-SW	Sinistral Strike Slip	F35
		150/90	Dextral Strike Slip	F36
	-	NW-SE	Dextral Strike Slip with reverse component	F37

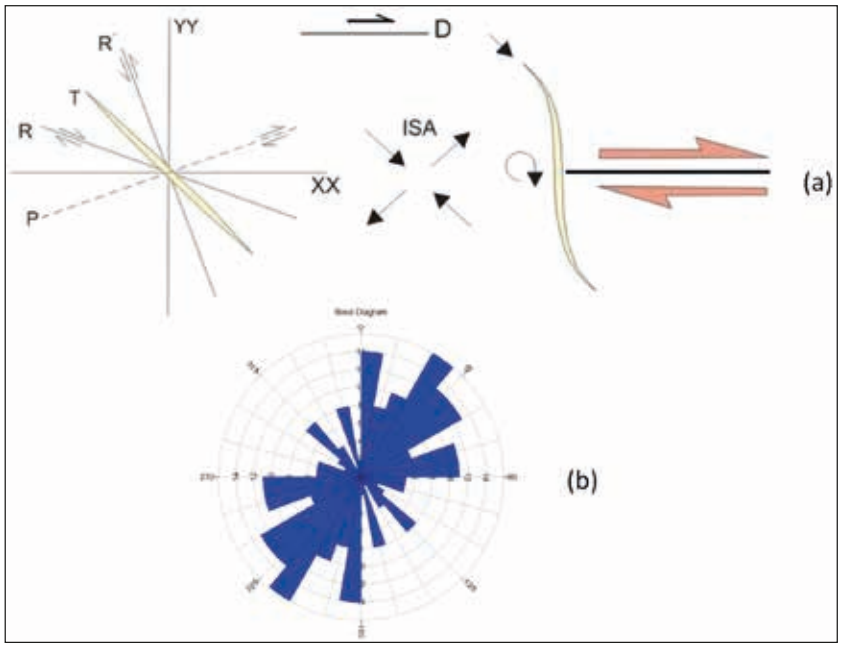

Fig. 4 - Correlation between Riedel shear patterns and faults of the studied area (a) and rose diagram for faults in the Gazestan deposit (b).

faults were compared and correlated with Riedel shear patterns (McClay and Bonora, 2001). Fig. 4 shows synthetic strike-slip faults named P and R shears with 15° angle from the main fault and antithetic strike-slip faults including R and R¢ shears, with 75° angle with the main fault direction. Nabilou (2017) proposed that the space between R and R¢ shear structures is effectively an ore fluids passage. As there are extensive alteration zones and fault displacements, it is highly likely that these faults play a significant role in the ore-forming processes in the area. Fig 4 shows that the dominant Gazestan deposit fault strike orientation is NW-SE, while the joints in the area point to an E-W stress direction. These stress systems have also displaced the magnetite orebodies along the NE-SW direction (Nabilou, 2017; Nabilou *et al.*, 2017; Soltani *et al.*, 2019).

2.3. Mineralisation and alteration

The Gazestan Fe-P-REE mineralisation is about 2.2 km long and >0.7 km wide (Parsi Kankav Consultant Engineers Co., 2015; Soltani *et al.*, 2019). The major ore mineral (Fig. 6) is magnetite with hematite as a result of martitisation and minor apatite, pyrite, and chalcopyrite (Afzali *et al.*, 2017). Based on the Scanning Electron Microscope-Energy Dispersion Spectrometry (SEM-EDS) studies, the apatite is mainly fluorapatite, with REE inclusions generally monazite, xenotime and allanite (Fig. 6). The REE mineral analyses show a large ratio of light REE / heavy REE and Eu depletion.

The host rock of the Gazestan deposit is greenish chlorite-epidote-sericite metasomatised felsic volcanics, invaded by a series of younger doleritic dikes. The Gazestan ore mainly consists of magnetite and apatite lenses, irregular bodies, veins, veinlets, and disseminated ore. The majority of magnetites are altered to hematite (martitisation). The main alterations (Fig. 5) are sodic-calcic alteration, sericitisation, silicification, chloritisation, and argillic alteration, which are spatially associated with fractures and faults (Afzali *et al.*, 2014; Nabilou, 2017; Soltani *et al.*, 2019).

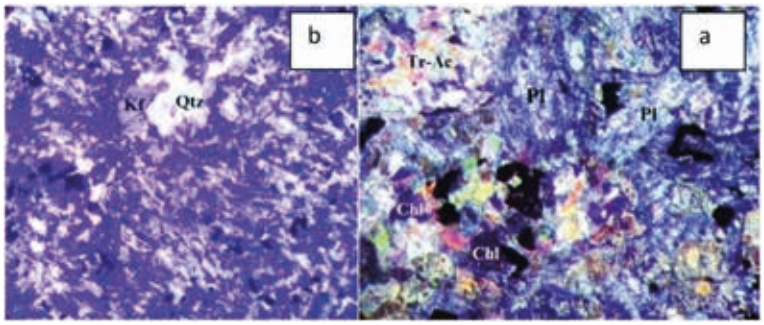

Fig. 5 - Alterations in the thin sections (Afzali *et al.*, 2017): a) chloritic (Chl) with actinolite (Ac) and Pl (plagioclase); and b) silicification (Qtz) and potassic (Kf).

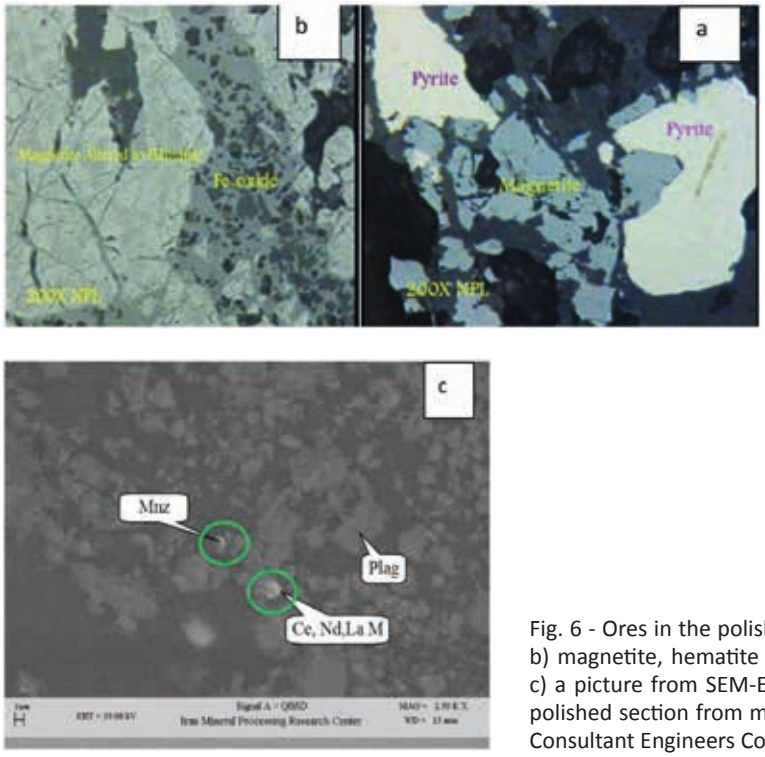

Fig. 6 - Ores in the polished sections: a) magnetite and pyrite; b) magnetite, hematite and Fe-oxide (Afzali *et al.*, 2017) and c) a picture from SEM-EDS for monazite (Mnz) and REEs in a polished section from magnetite-apatite sample (Parsi Kankav Consultant Engineers Co., 2015).

3. Data and methods

3.1. Concentration-Distance to Fault fractal model

Distance to fault fractal model is an effective tool to recognise geochemical anomalies and mineralised zones as the faults can play an important role. This method can also differentiate faults effectively involved in mineralisation. The Concentration-Distance to Fault (C-DF) fractal model, proposed by Nouri *et al.* (2013), has the following formula:

$$DF(\geq \rho) \propto F\rho^{-D} \quad (1)$$

where ρ is elemental concentration, $DF(\geq\rho)$ is the cumulative distance from the faults of sampled sites with concentration values equal, or greater than, ρ, F is a constant, and D is the scaling exponent or fractal dimension of the distribution of elemental grades (Adib *et al.*, 2021).

The faults data used in this model were drawn from two sources: the 1:500 Gazestan deposit surface geology map (named as 'surface faults', SF), and magnetic survey data (named as 'major magnetic faults', MBF). The distances to these faults are hence named DSF and DMBF, and the related REE mineralisation was classified accordingly.

The C-DMBF (Concentration-Distance to Major Magnetic Faults) and the C-DSF (Concentration-Distance to Surface Faults) were determined based on the REE concentrations in the exploration boreholes and the 2D and 3D structural model of the ore deposit. The 3D fault model was consequently generated using the C-DMBF fractal model, to determine the relationship between mineralisation and faults. The workflow of this process is illustrated in Fig. 7.

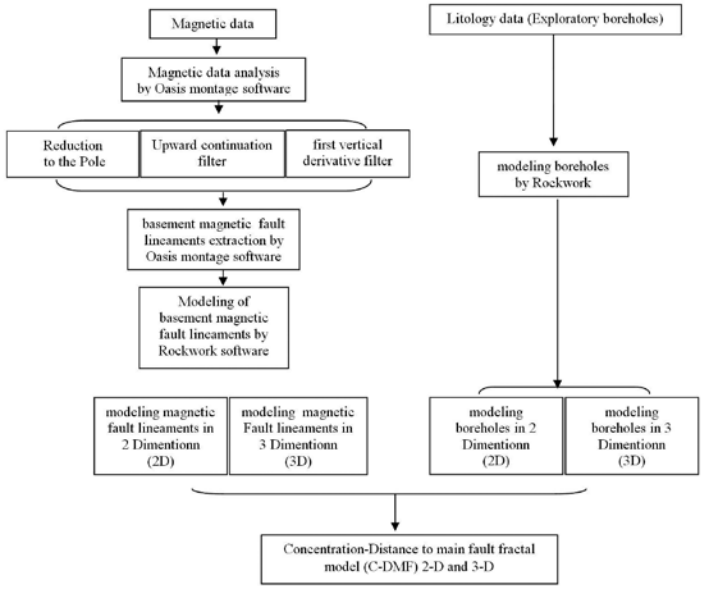

Fig. 7 - The procedure of this research.

3.2. Magnetic data

In order to plot the magnetic faults, two sets of airborne and ground survey magnetic data were used. The airborne magnetic data have a nominal flight altitude of 120 m and a flight line spacing of 500 m with N45º azimuth. These data were collected by the Iranian Atomic Energy Organization between 1974 and 1979. The airborne magnetic data were corrected for the diurnal variations, International Geomagnetic Reference Field (IGRF) model of 1975 removal, and were levelled using timeline data, as shown in Fig. 8. The ground magnetic data were collected by the Geological Survey of Iran (GSI) in 2003, using a proton magnetometer. The studied area was surveyed by 49 profiles with N-S direction and 25-m spacing. There are 53 survey points on each profile with 10-m sample interval.

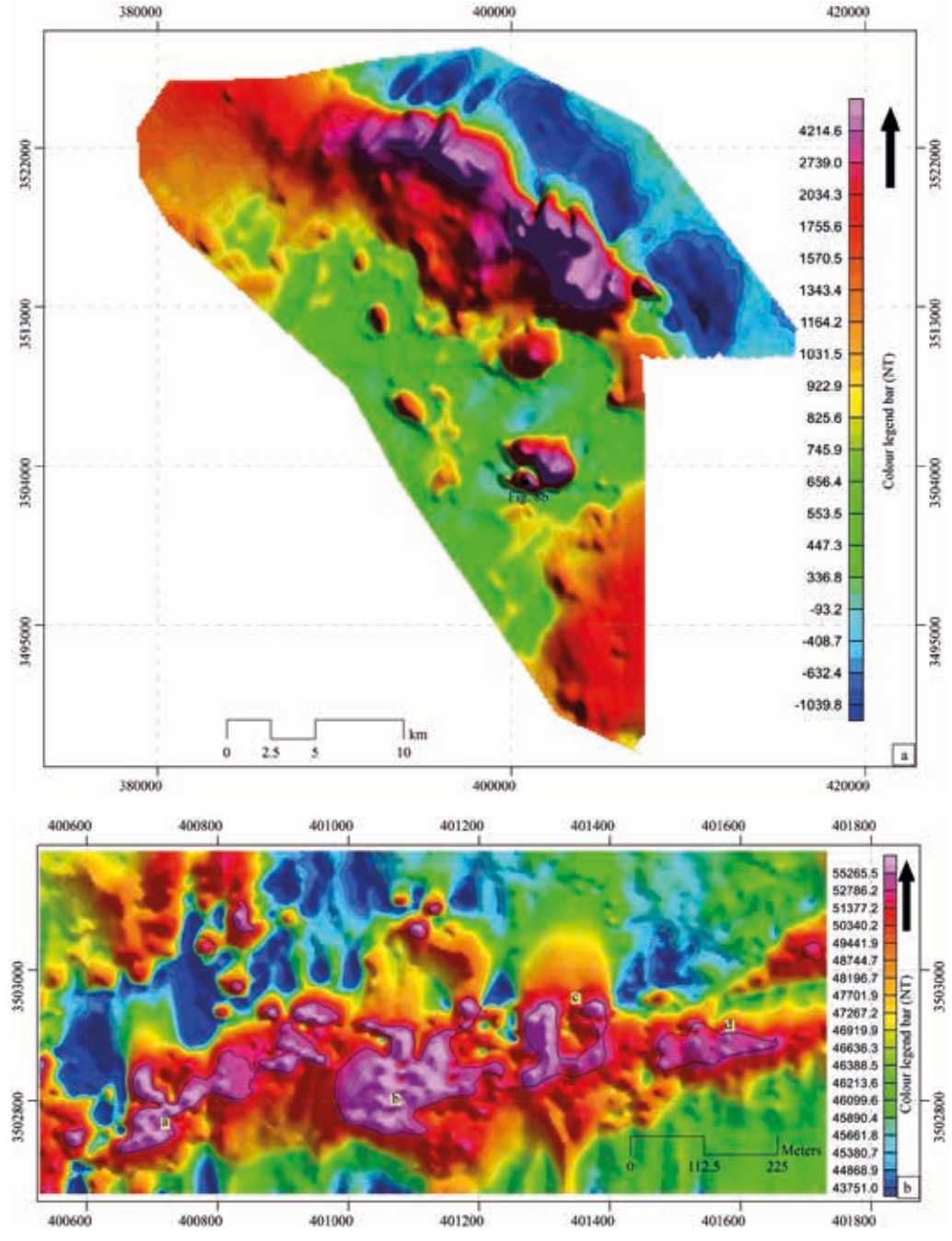

Fig. 8 - Regional (a) and ground magnetic (b) maps of the Gazestan deposit. High-density anomalies are shown by the polygons *a*, *b*, *c* and polygon on the map of the Gazestan deposit.

3.3. Exploratory boreholes

The subsurface data were obtained from 34 exploratory boreholes, drilled by GSI in 1998 and Parsi Kankav Consulting Engineers Co. (2015). The total length of these drill holes is 6133.3 m and the maximum depth of boreholes is 350 m. All the samples were analysed by induced

coupled plasma-mass spectrometry method in the Iranian Mineral Processing Centre. All interpreted faults and the borehole REE geochemical data were mapped and used to determine the relationship between the major fault and the REE mineralisation.

3.4. Magnetic data analysis

3.4.1. Reduction to the pole

Reduction to the pole (RTP) filter enhances the magnetic data by removing the dependency of the magnetic data on the magnetic inclination and by transforming the data to a magnetic pole, where the magnetic field is vertical. This filter simplifies the interpretation of the data for sub-vertical prisms or sub-vertical contacts (including faults) and transforms their asymmetric responses to simple symmetric and asymmetric forms. The symmetric highs are directly centred on the target body, while the maximum gradient of the asymmetric dipolar anomalies coincides exactly with the body edges (Almasi *et al.*, 2014). This transformation is usually necessary for magnetic data at low latitudes. The RTP was performed on the digitised aeromagnetic data of the study area via Fast Fourier Filtering programs to remove the dipolar nature of the magnetic field. The regional and deposit-scale RTP magnetic maps of the study area are illustrated in Fig. 8. Fig. 8a shows the magnetic anomaly map of the Gazestan deposit, where the high magnetic anomalies are related to iron ores and mafic rocks.

3.4.2. Major magnetic faults extraction

The upward continuation method is a mathematical technique to adjust the altitude of magnetic intensity data to a datum as an aid to the magnetic data interpretation, reducing short-wavelength noise by continuing the field upwards, and increasing the horizontal resolution of anomalies and their sources by continuing the field downwards. The outcome of this technique is smoothing the short-wavelength features on moving away from the anomaly. As a result, this process can enhance large-scale features such as large and deep faults and enhance anomalies caused by deep sources at the expense of anomalies caused by shallow sources (Mekonnen, 2004; Ravat, 2007).

Therefore, to calculate the field at a higher level using the knowledge of the field at a lower level, we need to use numerical integration of the surface data, i.e. the computations are made by replacing the surface integral with a weighted sum of values taken on a regular grid (Ganiyu *et al.*, 2013).

The First Vertical Derivative (FVD) filter was applied on the upward continuation results. The range of the magnetic field intensity gradient in different directions tends to sharpen the edges of anomalies and detect surface anomalies (Feumoe *et al.*, 2012). The vertical derivative map is much more responsive to local influences than to broad or regional effects and, therefore, tends to offer a sharper picture compared to the map of the total field intensity. As a result, the smaller anomalies will be clearer in areas of strong regional disturbances. The FVD is used to delineate high-frequency features more precisely, where they are shadowed by large-amplitude, low-frequency anomalies. The enhancement of magnetic anomalies associated with faults and other structural discontinuities was outlined by the application of the FVD to the residual map in Figs. 9 and 10 (Dobrin and Savit, 1988). The reprocessed magnetic data set is significantly enhanced in high frequencies and is much better suited to detailed regional shallow (near-surface) mapping and analysis of major magnetic boundaries.

In the case of the Gazestan deposit, the ground magnetic data were used and the combination of the RTP upward continuation (Ganiyu *et al.*, 2013) and FVD (Telford *et al.*, 1990) filters were

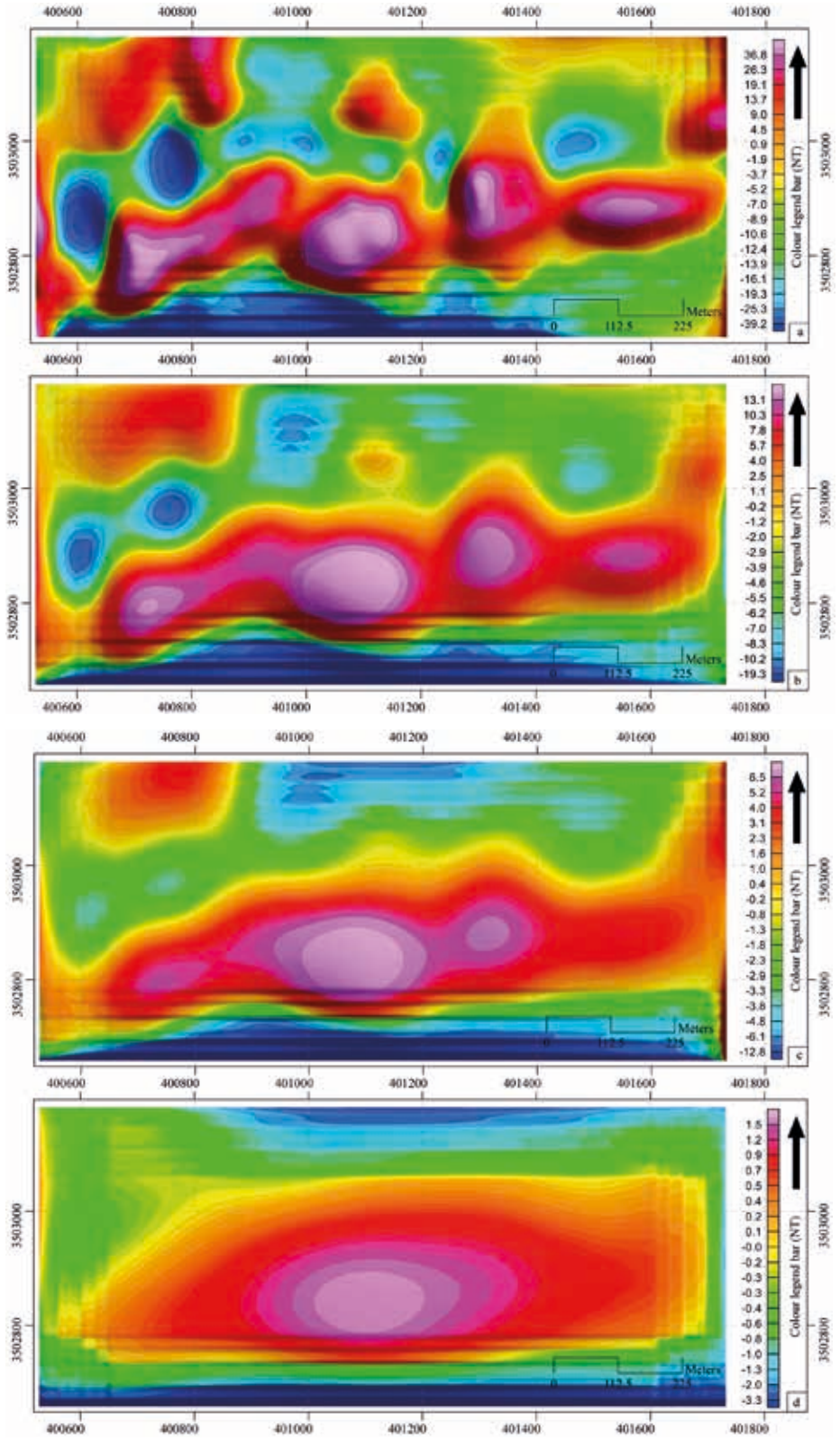

Fig. 9 - The FVD of upward continuations of 50 m (a), 100 m (b), 150 m (c), and 300 m (d) in the Gazestan deposit.

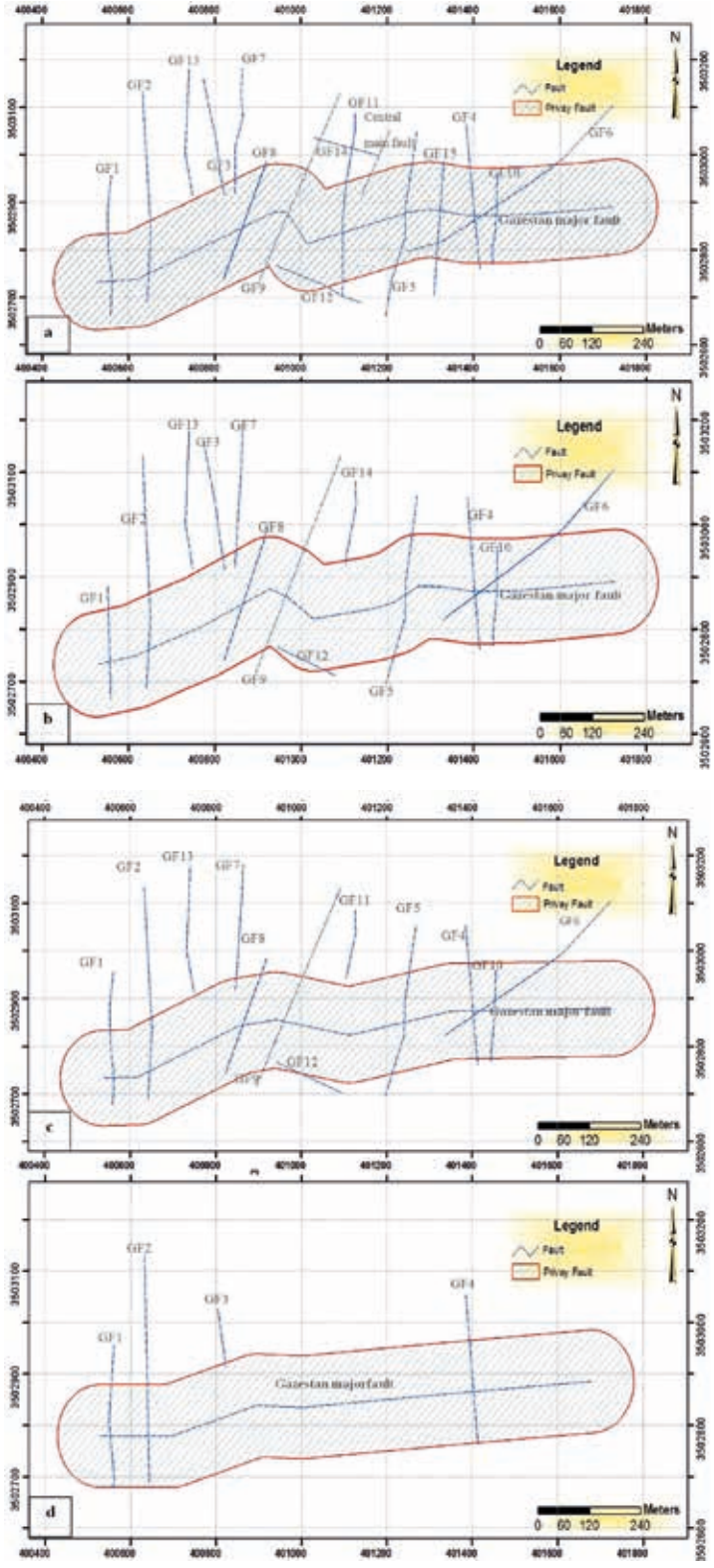

Fig. 10 - Maps of major faults extracted from ground geophysical data, based on upward continuation and FVD filters in the levels of 50 m (a), 100 m (b), 150 m (c), and 300 m (d).

applied to delineate structures at the depths of 50, 100, 150, 300, and 500 m beneath the surface (Fig. 9). Then, the result was incorporated with the colour-shaded grid image using the Oasis Montaj software. The results of this method are used to build a structural model for a deeper understanding of the subsurface structure in the studied area. The Gazestan major structures are extracted by horizontal or vertical displacements and sudden changes in the direction of magnetic anomalies in 2D and 3D models (Figs. 10 to 13). Based on magnetic anomaly maps, there are two types of structures recognised: the primary (main structures) and the secondary structures. With increasing depth, the magnetic traces of the secondary structures become less apparent (Figs. 9 and 10). The Gazestan main structures are recognised as suitable features for further fractal REE distribution modelling.

3.5. Application of the C-DMF fractal model

In this research, the C-DMF fractal model was adopted to investigate the relationship between REE distribution and the major magnetic fault extracted from 1:500 Gazestan geological and

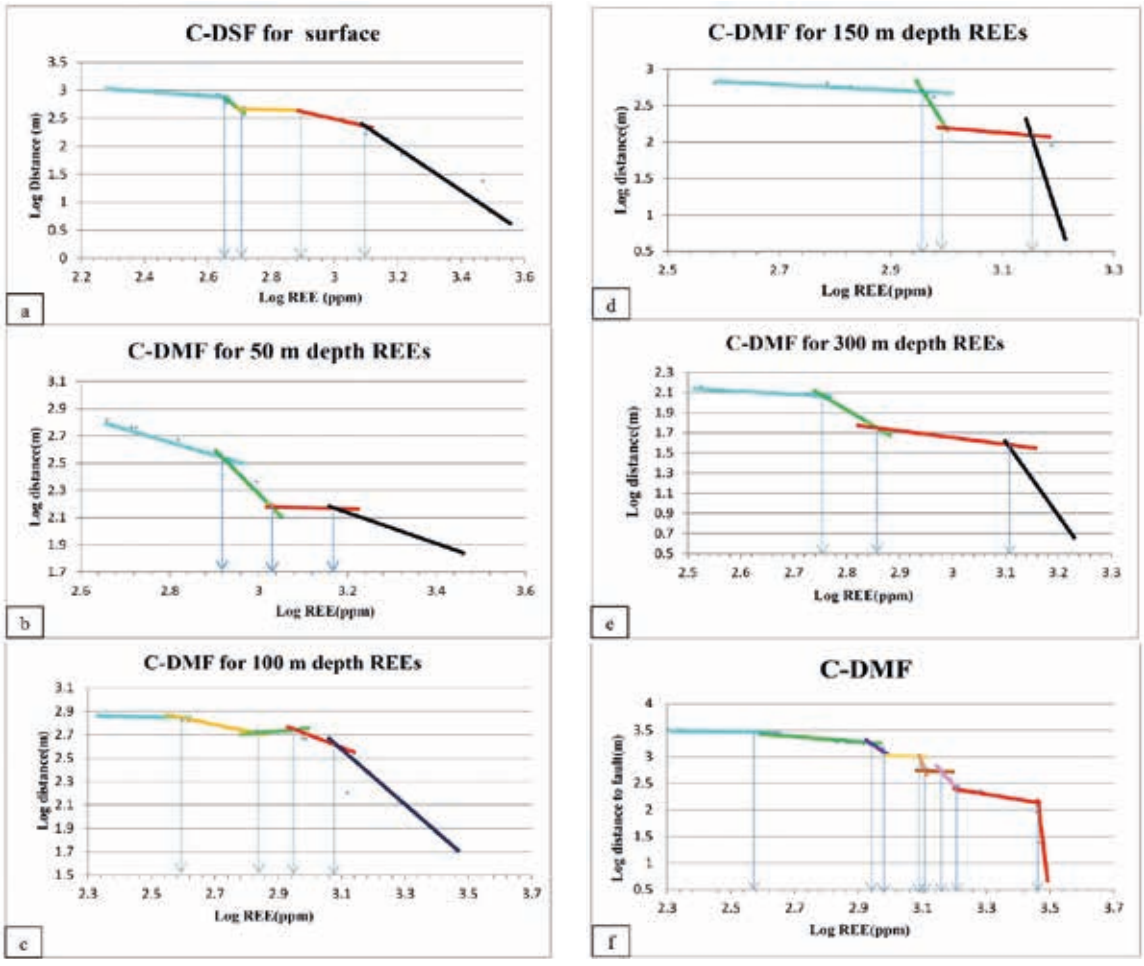

Fig. 11 - The C-DSF and C-DMF fractal diagrams of exploratory boreholes for REEs in the horizons of surface (a), 50 m (b), 100 m (c), 150 m (d), 300 m (e), and combination (f) of all horizons (surface, 50, 100, 150, and 300 m) of the entire depth of the Gazestan deposit.

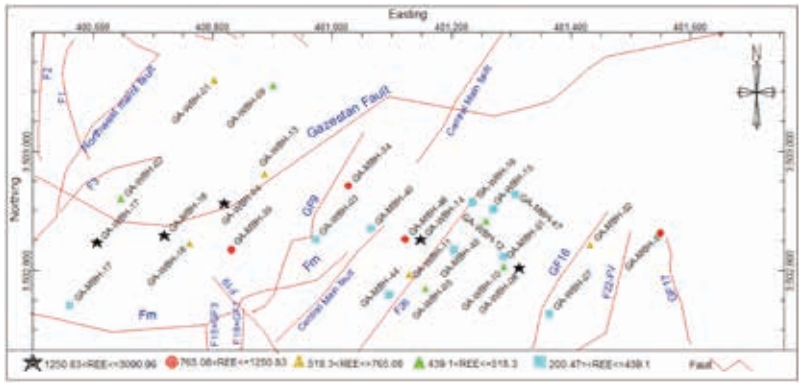

Fig. 12 - C-DMF fractal map for REEs in the surface of the Gazestan deposit.

magnetic map. The faults extracted from the geology map were confirmed by the processed magnetic anomaly map. The REE concentrations at the depths of 0, 50, 100, 150, and 300 m and their distance to closest major magnetic faults in both horizontal and vertical directions were used to generate C-DSF and C-DMF results for each borehole. These results are summarised in Table 2.

As Fig. 11 shows, the REE concentration in the boreholes increases with proximity to faults. The fractal model of the REE grades for the depth of 0, 50, 100, 150, and 300 m and the 'distances to the nearest major fault' using C-DSF and C-DMF model are presented in Figs. 12 to 14.

4. Discussion and results

The major high-magnetic anomalies namely *a*, *b*, *c* and *d* are shown in Fig. 8b. The comparison of magnetic and geological maps shows that the major part of a magnetic anomaly in the deposit area is related to medium- to high-grade magnetite and apatite mineralisation, which occurred in green to dark-green metasomatised basalt of Cambrian age ($Є_{mb}$ unit).

Anomaly *b* does not have any outcrop on geology units. It can be correlated with metasomatised basalt and grey to red fine-grained to porphyry andesite to andesite basalt (Cambrian units) with strong iron-oxide alteration.

The large part of anomaly *c* corresponds with medium- to high-grade magnetite and apatite mineralisation, which occurred in Єmb unit. Most of the anomaly *d* is located on Quaternary units (Q_{al}), but it seems that is related to $Є_{mb}$ units.

The REE concentrations of 0, 50, 100, 150, and 300 m depth horizons (Figs. 12 and 13) were used for individual boreholes and each horizon was mapped with a logarithmic diagram model of C-DMF to the major faults.

Based on Fig. 11, the C-DSF and C-DMF log-log plots represent a multifractal nature. The high REE values have distances of 6 m < DSF ≤ 220 m from the nearest surface fault (Table 2 and Fig. 11). Based on the C-DMF model, the high REE concentrations of 1474-2879 ppm, 1187-2870 ppm, 1419-1628 ppm, and 1295-1597 ppm are located in a cumulative distance of 50-409, 66.8-146, 5-121, and 7-38 m to the Gazestan main fault at the horizons of 50, 100, 150, and 300 m depth, respectively. According to the C-DSF model, the cumulative distance of high concentrations of REE mineralisation (1251-3091 ppm) is less than 220 m to the closest surface fault. The C-DMBF modelling for the 3D environment from the surface to the depth of 500 m shows two major

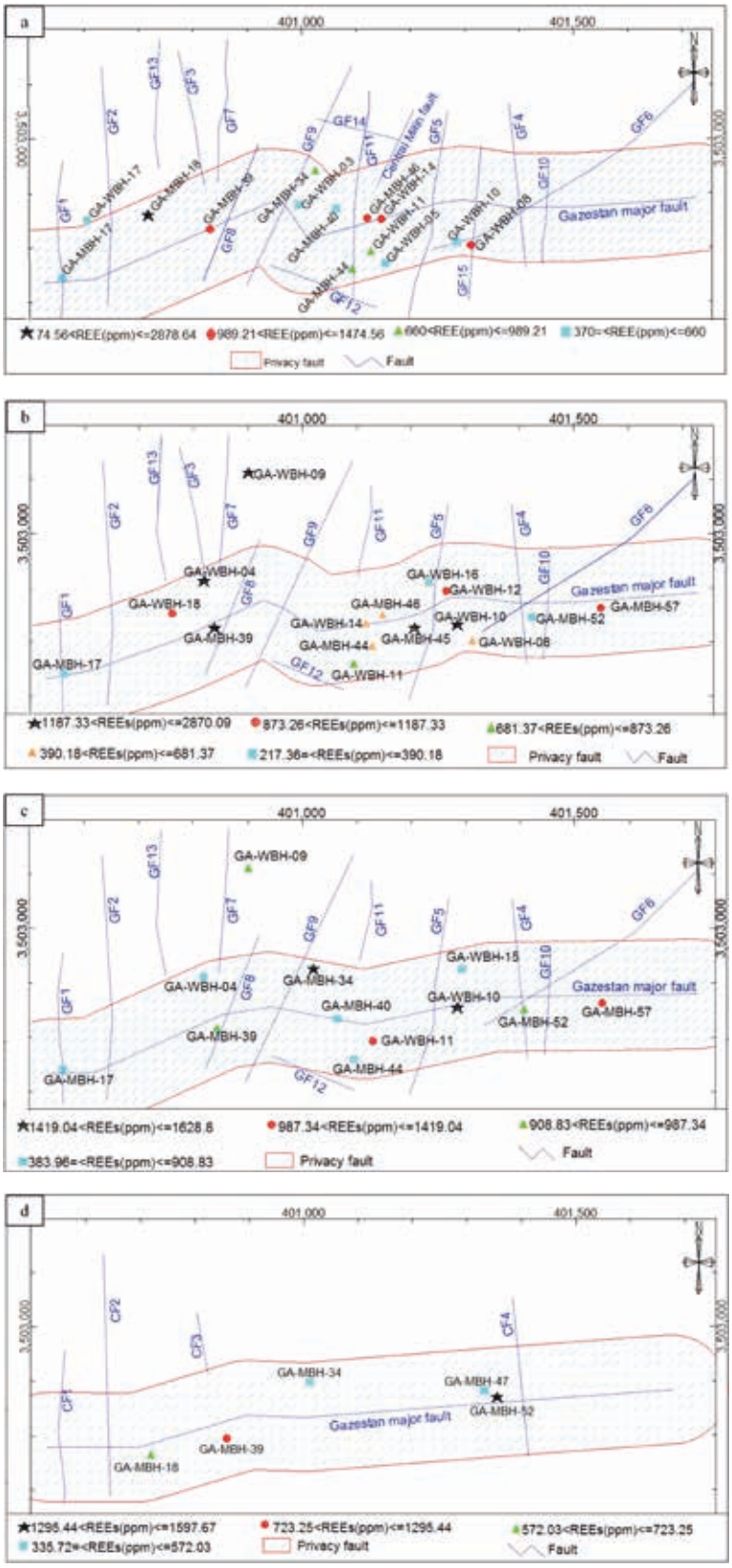

Fig. 13 - The C-DMBF fractal map in comparison with REEs in the horizons of 50 m (a), 100 m (b), 150 m (c), and 300 m (d) at the Gazestan deposit.

Table 2 - The components of C-DMF model in the Gazestan deposit.

C-DMF Component for REE																
BH-ID		Surface			50 m Depth			100 m Depth			150 m Depth			300 m Depth		
	REE(ppm)	Distance to fault	Nearest Fault	population line color	REE(ppm)	Distance to Gazestan major fault	population line color	REE(ppm)	Distance to Gazestan major fault	population line color	REE(ppm)	Distance to Gazestan major fault	population line color	REE(ppm)	Distance to Gazestan major fault	population line color
GA-WBH-04	3,090.96	6.70	Gazestan major fault	Black				1937.27		Black	672.53	76.00	Blue			
GA-MBH-18	2,943.31	17.30	Gazestan major fault	Black	2,878.64	66.80	Black							723.25	19	Green
GA-WBH-17	1,634.97	48.60	Gazestan major fault	Black	660.2	106.40	Blue									
GA-WBH-08	1,474.56	64.50	GF16	Black	1,474.56	79.8	Red	413.42		Orange						
GA-WBH-14	1,256.57	30.00	F26	Black	1,256.57	0.00	Red	394.91		Orange						
GA-MBH-39	1,250.83	53.30	Gazestan major fault	Red	1,439.80	0.00	Red	1908.45		Black	987.34	18.90	Red	1295.44	31	Red
GA-MBH-57	1,233.59	22.80	GF17	Red				1187.33		Red	1,261.47	13.70	Green			
GA-MBH-46	1,078.23	44.90	Central major fault	Red	1,078.23	9.20	Red	681.37		Orange						
GA-MBH-34	1,047.66	24.20	GF9	Red	861.24	85.30	Green				1,543.98	83.50	Black	572.03	62	Blue
GA-WBH-01	765.08	102.60	Northwest majort fault	Orange												
GA-WBH-18	746.57	8.80	Gazestan major fault	Orange				970.72		Red						
GA-WBH-13	740.4	12.00	Gazestan major fault	Orange												
GA-MBH-52	732.68	10.30	GF16	Orange				217.36		Blue	919.31	22.50	Blue	1597.67	7.3	Black
GA-WBH-11	654.03	8.10	F26	Orange	824.71	49.60	Green	561.48		Green	1,419.04	32.00	Blue			
GA-WBH-05	518.3	27.30	F26	Green	530.64	81.30	Blue									
GA-WBH-10	456.6	88.60	GF16	Green	456.6	75.80	Blue	2870.09		Black	1,628.80	5.90	Blue			
GA-WBH-12	456.6	36.90	F26	Green				950.16		Red						
GA-WBH-02	450.43	36.00	Gazestan major fault	Green												
GA-WBH-09	450.43	125.80	Gazestan major fault	Green				1233.95		Black	950.16	257.20	Green			
GA-MBH-45	439.1	26.00	F26	Blue				1312.67		Black						
GA-WBH-03	431.93	8.30	GF9	Blue	567.65	21.00	Blue									
GA-MBH-44	423.53	14.00	F26	Blue	989.21	76.00	Green	873.26		Orange	908.83	65.00	Green			
GA-WBH-16	388.74	2.00	F26	Blue				390.18		Blue						
GA-WBH-07	376.4	14.30	GF16	Blue												
GA-MBH-40	370.82	8.30	Central major fault	Blue	370.82	43.00	Blue				868.83	0.00	Red			
GA-WBH-15	333.21	32.80	F26	Blue							610.84	62.80	Blue			
GA-MBH-47	242.13	62.00	F26	Blue										335.72	23	Blue
GA-MBH-51	225.97	96.70	GF16	Blue												
GA-MBH-17	200.47	2.80	Fm	Blue	519.34	6.90	Blue	336.85		Blue	383.96	7.50	Black			

phases for REE mineralisation. The main REE mineralisation occurred with 2870-3091 ppm at 6-90 m cumulative distance to the Gazestan main fault. The density of faults is higher in the western part of the Gazestan deposit and, as a result, most of the high-grade REE ores are in the western parts of the deposit, as shown in Fig. 14. As seen in the 3D plots of the C-DMBF model,

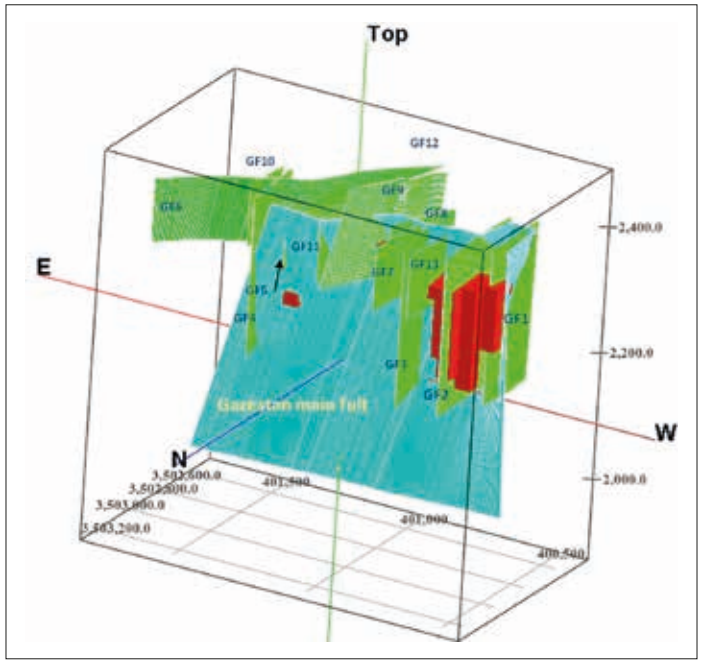

Fig. 14 - The C-DMF fractal for a 3D model based on a high grade of REEs as red voxels in combination with 3D faults in the Gazestan deposit.

the cumulative distances of high values of REEs in the total horizons of 50, 100, 150, and 300 m depth (2870-3091 ppm) are located lower than 90 m to the main faults. As observed in the 2D map and 3D block model, the REEs are generally accumulated along the primary main fault and secondary faults with W-SW trends at depths of more than 150 m (Figs. 13 and 14).

For the validation of the results, five samples were collected from high-grade REE zones and studied by scanning electron microscope. These samples contain grades of REEs between 446 ppm and 0.45% within monazites and xenotimes. There are high values of Ce, La, and Nd (Parsi Kankav Consultant Engineers Co., 2015).

5. Conclusions

The results of C-DSF and C-DMBF fractal models in the Gazestan Fe-Oxide-P-REE deposit reveal a clear relationship between REE mineralisation and major magnetic faults. These models show a direct relationship between increasing REE concentration in boreholes and the proximity to the main faults. Furthermore, based on the C-DMF model, the cumulative distances of high concentrations of 1474-2878.64, 1187-2870, 1419-1628, and 1295-1597 ppm of REE mineralisation at 50, 100, 150, and 300 m depth horizons are lower than 409, 146, 121, and 38 m to the main faults. The 3D map of the C-DMBF model suggests that the distances of high-grade REE ore to nearest faults in the total horizons of 50, 100, 150, and 300 m depth are less than 90 m to the main fault.

Based on the fractal modelling results, the high REE concentrations occurred close to the Gazestan main fault, the main major magnetic reverse fault in the area, which is traceable from the surface to the depth of 300 m.

These proposed fractal models in the Gazestan deposit can be used as an effective exploration tool in similar hydrothermal mineralisation scenarios to determine their relationship with fault structures. This model has a particularly high value in Bafq-Saghand metallogenic block future exploration. Although it may be easier to study geochemical anomalies with the C-A method, the multifractal nature of C-D log-log plots could be of great help to geoscientists for interpreting the stages of elemental enrichments. The developments in this fractal modelling and their usage could provide a favourable field for the stochastic simulation of geochemical distributions, and enhance their understanding.

REFERENCES

Adib A., Afzal P., Mirzaei Ilani S. and Aliyari F.; 2017a: *Determination of the relationship between major fault and zinc mineralization using fractal modeling in the Behabad Fault zone, central Iran*. J. Afr. Earth Sci., 134, 308-319.

Adib A., Mirzaei Ilani S., Shoaei G. and Afzal P.; 2017b: *Determination of a conceptual model for the structural features and Pb-Zn mineralization in the north of Behabad Fault zone, central Iran*. Iran. J. Earth Sci., 9, 168-183.

Adib A., Nabilou M. and Afzal P.; 2021: *Relationship between Fe-Cu-REEs mineralization and magnetic basement faults using multifractal modeling in Tarom region, NW Iran.* Episodes, in press.

Afzal P., Fadakar Alghalandis Y., Khakzad A., Moarefvand P. and Rashidnejad Omran N.; 2011: *Delineation of mineralization zones in porphyry Cu deposits by fractal concentration-volume modeling.* J. Geochem. Explor., 108, 220-232.

Afzal P., Fadakar Alghalandis Y., Moarefvand P., Rashidnejad Omran N. and Asadi Haroni H.; 2012: *Application of power-spectrum-volume fractal method for detecting hypogene, supergene enrichment, leached and barren zones in Kahang Cu porphyry deposit, central Iran.* J. Geochem. Explor., 112, 131-138.

Afzal P., Ahmadi K. and Rahbar K.; 2017: *Application of fractal-wavelet analysis for separation of geochemical anomalies*. J. Afr. Earth Sci., 128, 27-36.

Afzal P., Adib A. and Ebadati N.; 2018: *Delineation of seismic zonation using fractal modeling in west Yazd province, central Iran*. J. Seismolog., 22, 1377-1393.

Afzali S., Nezafati N., Ghaderi M., Ghalamghash J., Ghassemi M.R. and Karimi Bavandpur A.; 2014: *Petrogenesis and mineralization at Gazestan iron oxide-apatite deposit, east of Bafq, central Iran*. Sci. J. Quarterly Geosci., 24, 77-84, in Persian with English abstract.

Afzali S., Nezafati N. and Ghaderi M.; 2017: *Fluid inclusion and stable isotope study of the Gazestan magnetite-apatite deposit, central Iran.* Sci. J. Quarterly Geosci., 26, 35-44, in Persian with English abstract.

Agterberg F.P.; 1995: *Multifractal modeling of the sizes and grades of giant and supergiant deposits*. Int. Geol. Rev., 37, 1-8.

Agterberg F.P., Cheng Q., Brown A. and Good D.; 1996: *Multifractal modeling of fractures in the Lac du Bonnet Batholith, Manitoba*. Comput. Geosci., 22, 497-507.

Ahmadfaraj M., Mirmohammadi M., Afzal P., Yasrebi A.B. and Carranza E.J.; 2019: *Fractal modeling and fry analysis of the relationship between structures and Cu mineralization in Saveh region, central Iran*. Ore Geol. Rev., 107, 172-185.

Alaminia Z., Tadayon M., Finger F., Lentz D.R. and Waitzinger M.; 2020: *Analysis of the infiltrative metasomatic relationships controlling skarn mineralization at the Abbas-Abad Fe-Cu deposit, Isfahan, north Zefreh Fault, central Iran.* Ore Geol. Rev., 117, 103321.

Alipour Shahsavari M., Afzal P. and Hekmatnejad A.; 2020: *Identification of geochemical anomalies using fractal and LOLIMOT neuro-fuzzy modeling in Mial area, central Iran*. J. Min. Environ., 11, 99-117.

Aliyari F., Afzal P., Lotfi M., Shokri S. and Feizi H.; 2020: *Delineation of geochemical haloes using the developed zonality index model by multivariate and fractal analysis in the Cu-Mo porphyry deposits*. Appl. Geochem., 121, 104694, doi: 10.1016/j.apges chem.2020.104694.

Almasi A., Jafarirad A., Kheyrollahi H., Rahimi M. and Afzal P.; 2014: *Evaluation of structural and geological factors in orogenic gold type mineralization using airborne geophysical data, Kervian area, NW of Iran*. Explor. Geophys., 45, 261-270.

Carranza E.J.M.; 2009: *Controls on mineral deposit occurrence inferred from analysis of their spatial pattern and spatial association with geological features*. Ore Geol. Rev., 35, 383-400.

Carranza E.J.M.; 2010: *From predictive mapping of mineral prospectivity to quantitative estimation of number of undiscovered prospects*. Resour. Geol., 61, 30-51.

Chen F., Chen S. and Peng G.; 2013: *Using sequential gaussian simulation to assess geochemical anomaly areas of lead element*. In: Li D. and Chen Y. (eds), Computer and Computing Technologies in Agriculture VI - CCTA 2012, IFIP Advances in Information and Communication Technology, Springer, Berlin, Germany, Vol. 393, pp. 69-76, doi: 10.1007/978-3-642-36137-1_9.

Cheng Q.; 1999: *Multifractality and spatial statistics.* Computers & Geosciences, 25, 949-961.

Cheng Q.; 2007: *Mapping singularities with stream sediment geochemical data for prediction of undiscovered mineral deposits in Gejiu, Yunnan province, China.* Ore Geol. Rev., 32, 314-324.

Cheng Q., Agterberg F.P. and Ballantyne S.B.; 1994: *The separation of geochemical anomalies from background by Fractal method*. J. Geochem. Explor., 51, 109-130.

Cohen D.R., Kelley D.L., Anand R. and Coker W.B.; 2010: *Major advances in exploration geochemistry, 1998-2007.* Geochem. Explor. Environ. Anal., 10, 3-16.

Craw D. and Campbell J.R.; 2004: *Tectonic and structural setting for active mesothermal gold vein systems, southern Alps, New Zealand*. J. Struct. Geol., 26, 995-1005.

Daliran F.; 2002: *Kiruna type iron oxide-apatite ores and apatitites of the Bafq district, Iran, with an emphasis on the REE geochemistry of their apatites*. In: Porter T.M. (ed), Hydrothermal iron oxide copper-gold and related deposits: a global perspective, PGC Publishing, Adelaide, Australia, Vol. 1, pp. 303-320.

Daliran F., Stosch H.G. and Williams P.; 2007: *Multistage metasomatism and mineralization at hydrothermal Fe oxide-REE-apatite deposits and apatitites of the Bafq district, central-east Iran*. In: Proc. 9th Biennial Meeting, Andrew C.J. and Borg G. (eds), Digging Deeper, Society for Geology Applied to Mineral Deposits, Dublin, Ireland, pp. 1501-1504.

Daliran F., Stosch H.G. and Williams P.A.; 2009: *A review of the Early Cambrian magmatic and metasomatic events and their bearing on the genesis of the Fe oxide-REE-apatite deposits (IOA) of the Bafq district, Iran.* In: Proc. 10th Biennial Meeting, Williams P.J. and Rush B. (eds), Smart Science for Exploration and Mining, Society for Geology Applied to Mineral Deposits, Townsville, QLD, Australia, pp. 623-625.

Daliran F., Stosch H.G., Williams P., Jamali H. and Dorri M.B.; 2010: *Early Cambrian iron oxide-apatite-REE (U) deposits of the Bafq district, east-central Iran.* In: Corriveau L. and Mumin H. (eds), Exploring for iron oxide copper-gold deposits: Canada and global analogues, Geological Association Canada, St. John's, Newfoundland, Canada, Short Course Notes, 20, pp. 143-155.

Daneshvar Saein L. and Afzal P.; 2017: *Correlation between Mo mineralization and faults using geostatistical and fractal modeling in porphyry deposits of Kerman magmatic belt, SE Iran*. J. Geochem. Explor., 181, 333-343.

Davis J.C.; 2002: *Statistics and data analysis in geology*. John Wiley and Sons Inc., New York, NY, USA, 638 pp.

Deymar S., Yazdi M., Rezvanianzadeh M.R. and Behzadi M.; 2018: *Alkali metasomatism as a process for Ti-REE-Y-U-Th mineralization in the Saghand anomaly 5, central Iran: insights from geochemical, mineralogical, and stable isotope data*. Ore Geol. Rev., 93, 308-336.

Dobrin M.B. and Savit C.H.; 1988: *Introduction to geophysical prospecting*. McGraw-Hill, New York, NY, USA, 867 pp.

Dori M.B. and Jamali H.; 2003: *The exploratories report of the general level (semi-detailed) in phosphate REEs deposit.* Geological Survey of Iran, Tehran, Iran, 110 pp.

Dori M.B., Sepehri Rad R. and Jamali H.; 2008: *Report of detailed exploratories in phosphate REEs deposit*. Geological Survey of Iran, Tehran, Iran, 200 pp.

Drew L.J.; 2006: A *tectonic model for the spatial occurrence of porphyry copper and polymetallic vein deposits - applications to central Europe*. USGS, Reston, VA, USA, Scientific Investigation Report, pp. 1-36.

Farahmandfar Z., Jafari M.R., Afzal P. and Ashja Ardalan A.; 2019: *Description of gold and copper anomalies using fractal and stepwise factor analysis according to stream sediments in NW Iran.* Geopersia**,** in press.

Feumoe A.N.S., Ndougsa-Mbarga T., Manguelle-Dicoum E. and Fairhead J.D.; 2012: *Delineation of tectonic lineaments using aeromagnetic data for the south-east Cameroon area.* Geofizika, 29, 175-192.

Forster H. and Jafarzade A.; 1994: *The Bafq mining district in central Iran - a highly mineralized infracambrian volcanic field.* Econ. Geol., 89, 1697-1721.

Fyzollahhi N., Torshizian H., Afzal P. and Jafari M.R.; 2018: *Determination of lithium prospects using fractal modeling and staged factor analysis in Torud region, NE Iran.* J. Geochem. Explor., 189, 2-10.

Ganiyu S.A., Badmus B.S., Awoyemi M.O., Akinyemi O.D. and Oluwaseun Olurin T.; 2013: *Upward continuation and reduction to pole process on aeromagnetic data of Ibadan area, south-western Nigeria*. Earth Sci. Res., 2, 66-73, doi: 10.5539/esr.v2n1p66.

Ghavami Riabi R.; 2006: *Geochemical exploration of base metal massive sulphide deposits in the eastern part of Namaqua province and environmental South Africa.* Ph.D. Thesis in Geological Sciences, Pretoria University, South Africa, 329 pp.

Glorie S., Hall J.W., Nixon A., Collins A.S. and Reid A.; 2019: *Carboniferous fault reactivation at the northern margin of the metal-rich Gawler Craton (South Australia): implications for ore deposit exhumation and preservation*. Ore Geol. Rev., 115, 103193.

Haghipour A.; 1974: *Etude geologique de la region de Biabanak-Bafq (Iran central); petrologie et tectonique du socle Precambrien et de sa couverture.* Ph.D. Thesis in Geological Sciences, Universite Scientifique et Medicale de Grenoble, France, 403 pp.

Haghipour A.; 1977: *Geological map of Posht-e-Badam area*. Geological Survey of Iran, Tehran, Iran.

Hajsadeghi S., Asghari O., Mirmohammadi M., Afzal P. and Meshkani S.A.; 2017: *Uncertainty-volume fractal model for delineating copper mineralization controllers using geostatistical simulation in Nohkouhi volcanogenic massive sulfide deposit, central Iran.* Maden Tetkik ve Arama Dergisi, 159, 1-10.

Hassanpour S. and Afzal P.; 2013: *Application of concentration-number (C-N) multifractal modeling for geochemical anomaly separation in Haftcheshmeh porphyry system, NW Iran*. Arabian J. Geosci., 6, 957-970.

Hawkes H.E. and Webb J.S.; 1979: *Geochemistry in mineral exploration, 2nd ed.* Academic Press, New York, 657 pp.

Heidarian H., Alirezaei S. and Lentz D.R.; 2017: *Chadormalu Kiruna-type magnetite-apatite deposit, Bafq district, Iran: insights into hydrothermal alteration and petrogenesis from geochemical, fluid inclusion, and sulfur isotope data*. Ore Geol. Rev., 83, 43-62.

Huckriede R., Kursten M. and Venzlaff H.; 1962: Zur geologie des gebiets zwischen Kerman und Saghand (Iran). Beih. Geol. Jb., Heft 51, 197 pp.

Jami M.; 2005: *Geology, geochemistry and evolution of the Esfordi phosphate iron deposit, Bafq area, central Iran.* Ph.D. Thesis in Geological Sciences, The University of New South Wales, Sydney, Australia, 355 pp., unpublished.

Jami M., Dunlop A.C. and Cohen D.R.; 2007: *Fluid inclusion and stable isotope study of the Esfordi apatite-magnetite deposit, central Iran*. Econ. Geol., 102, 1111-1128.

Journel A.G.; 1993: *Geostatistics: roadblocks and challenges*. In: Soares A. (ed), Geostatistics Tróia '92, Quantitative Geology and Geostatistics, Springer, Dordrecht, The Netherlands, Vol. 5, pp. 213-224, doi: 10.1007/978-94-011-1739-5_18.

Karaman M., Kumral M., Yildirim D.K., Doner Z., Afzal P. and Abdelnasser A.; 2021: *Delineation of the porphyry-skarn mineralized zones (NW Turkey) using concentration-volume fractal model.* Geochem., 81, 125802, doi: 10.1016/j.chemer.2021.125802.

Khalajmasoumi M., Sadeghi B., Carranza E.J.M. and Sadeghi M.; 2016: *Geochemical anomaly recognition of rare earth elements using multi-fractal modeling correlated with geological features, central Iran.* J. Geochem. Explor., 181, 318-332.

Kouhestani H., Ghaderi M., Afzal P. and Zaw K.; 2020: *Classification of pyrite types using fractal and stepwise factor analyses in the Chah Zard gold-silver epithermal deposit, central Iran.* Geochem. Explor. Environ. Anal., 20, 496-508.

Lam N.S.; 1983: *Spatial interpolation methods: a review.* Am. Cartographer, 10, 129-149.

Li C., Ma T. and Shi J.; 2003: *Application of a fractal method relating concentrations and distances for separation of geochemical anomalies from background.* J. Geochem. Explor., 77, 167-175.

Lima A., De Vivo B., Cicchella D., Cortini M. and Albanese S.; 2003: *Multifractal IDW interpolation and fractal filtering method in environmental studies: an application on regional stream sediments of (Italy), Campania region.* Appl. Geochem., 18, 1853-1865.

Liu Y., Xia Q. and Carranza E.J.M.; 2019: *Integrating sequential indicator simulation and singularity analysis to analyze uncertainty of geochemical anomaly for exploration targeting of tungsten polymetallic mineralization, Nanling belt, south China.* J. Geochem. Explor., 197, 143-158.

Madani Esfahani N. and Asghari O.; 2013: *Fault detection in 3D by sequential Gaussian simulation of Rock Quality Designation (RQD).* Arabian J. Geosci., 6, 3737-3747.

Madani N. and Carranza E.J.M.; 2020: *Co-simulated size number: an elegant novel algorithm for identification of multivariate geochemical anomalies*. Nat. Resour. Res., 29, 13-40.

Mandelbrot B.B.; 1983: *The fractal geometry of nature, updated and augmented ed*. W.H. Freeman, San Francisco, CA, USA, 460 pp.

McClay K. and Bonora M.; 2001: *Analog models of restraining stopovers in strike-slip fault systems.* Am. Assoc. Pet. Geol. Bull., 85, 233-260.

Mehdipour Ghazi J., Harris C., Rahgoshay M. and Moazzen M.; 2019: *Combined igneous and hydrothermal source for the Kiruna-type Bafq magnetite-apatite deposit in central Iran; trace element and oxygen isotope studies of magnetite*. Ore Geol. Rev., 105, 590-604.

Mekonnen T.K.; 2004: *Interpretation and geodatabase of Dukes using aeromagnetic data of Zimbabwe and Mozambique.* M.Sc. Thesis in Applied Geophysics, International Institute for Geoinformation Science and Earth Observation, Enschede, the Netherlands, 80 pp.

Meng and Zhao P.; 1991: *Fractal method for statistical analysis of geological data.* Chin. J. Geosci., 2, 207-211.

Mohebi A., Mirnejad H., Lentz D., Behzadi M., Dolati A., Kani A. and Taghizadeh H.; 2015: *Controls on porphyry Cu mineralization around Hanza Mountain, south-east of Iran: an analysis of structural evolution from remote sensing, geophysical, geochemical and geological data*. Ore Geol. Rev., 69, 187-198.

Nabilou M.; 2017: *Structural modelling in Gazestan apatite-iron and rare elements deposit, Bafq, central Iran.* Ph.D. Thesis in Geological Sciences, Department of Geology, Science and Research Branch, Islamic Azad University, Tehran, Iran, 241 pp.

Nabilou M., Arian M., Afzal P., Adib A. and Kazemi Mehrnia A.; 2017: *The relationship between Fe mineralization and the basement linear structures using multifractal modelling in the Bafq area, central Iran.* Sci. J. Quarterly Geosci., 108, 181-190, in Persian with English abstract.

Nabilou M., Afzal P., Arian M., Adib A., Kheyrollahi H., Foudazi M. and Ansarirad P.; 2021: *The relationship between Fe mineralization and the magnetic basement structures using multifractal modeling in the Esfordi and Behabad areas (BMD), central Iran.* Acta Geologica Sinica, in press.

Nazarpour A.; 2018: *Application of C-A fractal model and Exploratory Data Analysis (EDA) to delineate geochemical anomalies in the: Takab 1:25,000 geochemical sheet, NW Iran.* Iran. J. Earth Sci., 10, 173-180.

Nouri R., Jafari M., Arain M., Feizi F. and Afzal P.; 2013: *Correlation between Cu mineralization and major faults using multifractal modeling in Tarom area, NW Iran*. Geol. Carpathica, 64, 409-416, doi: 10.2478/geoca-2013-0028.

Parsi Kankav Consultant Engineers Co.; 2015: *Final report of the exploration operation performance in Gazestan mining area, first published: topography and geology map.* Iranian Mines and Mining Industries Development and Renovation Organization (IMIDRO), Tehran, Iran, 123 pp.

Pourgholam M.M., Afzal P., Yasrebi A.B., Gholinejad M. and Wetherelt A.; 2021: *Detection of geochemical anomalies using a fractal-wavelet model in Ipack area, central Iran.* J. Geochem. Explor., 220, 106675.

Rajabi A.; 2012: *Ore controlling parameters and genesis of sedimentary-exhalative Zn-Pb (SEDEX type) deposits, Zarigan-Chahmir area, east of Bafq, central Iran.* Ph.D. Thesis in Geological Sciences, Tarbiat Modares University, Tehran, Iran, 420 pp.

Rajabi A., Rastad E., Alfonso P. and Canet C.; 2012: *Geology, ore facies and sulfur isotopes of the Koushk vent-proximal sedimentary-exhalative deposit, Posht-e-Badam block, central Iran.* Int. Geol. Rev., 54, 1635-1648, doi: 10.1080/00206814.2012.659106.

Rajabi A., Canet C., Rastad E. and Alfonso P.; 2015: *Basin evolution and stratigraphic correlation of sedimentary-exhalative Zn-Pb deposits of the Early Cambrian Zarigan-Chahmir basin, central Iran.* Ore Geol. Rev., 64, 328-353.

Ramezani J. and Tucker R.; 2003: *The Saghand region, central Iran: U-Pb geochronology, petrogenesis and implications for Gondwana tectonics.* Am. J. Sci., 303, 622-665.

Ravat D.; 2007: *Upward and downward continuation.* In: Gabbines D. and Herrero-Berrera E. (eds), Encyclopaedia of Geomagnetism and Paleomagnetism, Springer, Berlin, Germany, pp. 974-976.

Saadati H., Afzal P., Torshizian H. and Solgi A.; 2020: *Geochemical exploration for Li using Geochemical Mapping Prospectivity Index (GMPI), fractal and Stage Factor Analysis (SFA) in NE Iran.* Geochem. Explor. Environ. Anal., 20, 461-472.

Sadeghi B., Moarefvand P., Afzal P., Yasrebi A.B. and Daneshvar Saein L.; 2012: *Application of fractal models to outline mineralized zones in the Zaghia iron ore deposit, central Iran.* J. Geochem. Explor., 122, 9-19.

Sadeghi B., Khalajmasoumi M., Afzal P., Moarefvand P., Yasrebi A.B., Wetherelt A., Foster P. and Ziazarifi A.; 2013: *Using ETM+ and ASTER sensors to identify iron occurrences in the Esfordi 1:100000 mapping sheet of central Iran.* J. Afr. Earth Sci., 85, 103-114.

Samani B.A.; 1988: *Metallogeny of the Precambrian in Iran.* Precambrian Research, 39, 85-106.

Samani B.; 1993: *Saghand formation, a riftogenic unit of Upper Precambrian in central Iran.* J. Geosci., 6, 32-45.

Shahabpour J.; 2010: *Tectonic implications of the geochemical data from the Makran igneous rocks in Iran.* Island Arc, 19, 676-689, doi: 10.1111/j.1440-1738.2010.00723.x.

Shamseddin Meigooni M., Lotfi M., Afzal P., Nezafati N. and Kargar Razi M.; 2021a: *Application of multivariate geostatistical simulation and fractal analysis for detection of Rare Earth Elements (REEs) geochemical anomalies in Esfordi phosphate mine, central Iran.* Geochem. Explor. Environ. Anal., 21, 1-17, doi: 10.1144/geochem2020-035.

Shamseddin Meigooni M., Lotfi M., Afzal P., Nezafati N. and Kargar Razi M.; 2021b: *Detection of rare earth element anomalies in Esfordi phosphate deposit of central Iran, using geostatistical-fractal simulation*. Geopersia, 11, 115-130.

Soheili M. and Mahdavi M.A.; 1991: *Esfordi 1:100,000 geological sheet.* Geological Survey of Iran, Tehran, Iran.

Soltani F., Afzal P. and Asghari O.; 2014: *Delineation of alteration zones based on sequential Gaussian simulation and concentration-volume fractal modeling in the hypogene zone of Sungun copper deposit, NW Iran.* J. Geochem. Explor., 140, 64-76.

Soltani F., Moarefvand P., Alinia F. and Afzal P.; 2019: *Characterization of rare earth elements by coupling multivariate analysis, factor analysis, and geostatistical simulation; case-study of Gazestan deposit, central Iran.* **J**ournal of Mining and Environment, 10, 929-945.

Stosch H.G., Romer R.L., Daliran F. and Rhede D.; 2011: *Uranium-Lead ages of apatite from iron oxide ores of the Bafq district, east-central Iran.* Miner. Deposita, 46, 9-21.

Tahmasebi P. and Hezarkhani A.; 2012: *A hybrid neural networks-fuzzy logic-genetic algorithm for grade estimation.* Comput. Geosci., 42, 18-27.

Telford W.M., Geldart L.P. and Sheriff R.E.; 1990: *Applied geophysics 2nd ed.* Cambridge University Press, Cambridge, UK, 760 pp., doi: 10.1017/CBO9781139167932.

Turcotte D.L.; 1986: *A fractal approach to the relationship between ore grade and tonnage.* Econ. Geol., 18, 1525-1532.

Wang J. and Zuo R.; 2018: *Identification of geochemical anomalies through combined sequential Gaussian simulation and grid-based local singularity analysis.* Comput. Geosci., 118, 52-64.

Wang J. and Zuo R.; 2019: *Recognizing geochemical anomalies via stochastic simulation-based local singularity analysis.* J. Geochem. Explor., 198, 29-40.

Wang W., Zhao J., Cheng Q. and Liu J.; 2012: *Tectonic-geochemical exploration modeling for characterizing geo-anomalies in southeastern Yunnan district, China.* J. Geochem. Explor., 122, 71-80.

Yasrebi A.B. and Hezarkhani A.; 2019: *Resources classification using fractal modelling in eastern Kahang Cu-Mo porphyry deposit, central Iran.* Iran J. Earth Sci., 11, 56-67.

Yousefi M., Kamkar-Rouhani A. and Carranza E.J.M.; 2012: *Geochemical Mineralization Probability Index (GMPI): a new approach to generate enhanced stream sediment geochemical evidential map for increasing probability of success in mineral potential mapping.* J. Geochem. Explor., 115, 24-35.

Yousefi M., Kamkar-Rouhani A. and Carranza E.J.M.; 2014: *Application of staged factor analysis and logistic function to create a fuzzy stream sediment geochemical evidence layer for mineral prospectivity mapping.* Geochem. Explor. Environ. Anal., 14, 45-58.

Zuo R. and Wang J.; 2016: *Fractal/multifractal modeling of geochemical data: a review.* J. Geochem. Explor., 164, 33-41.

Zuo R., Xia Q. and Zhang D.; 2013: *A comparison study of the C-A and S-A models with singularity analysis to identify geochemical anomalies in covered areas.* Appl. Geochem., 33, 165-172.

Corresponding author: Peyman Afzal
Dpt. Geology, Science and Research Branch, Islamic Azad University
Western Fatemi, Tehran, Iran
Phone: +989 12345 0258; e-mail: p_afzal@azad.ac.ir